Synergistic effect of acidity and active phases on DBT hydrodesulfurization performance: the role of S-edge and Mo-edge sites

Zhengkai Cao[a,b], Xia Zhang[b*], Rong Guo[b], Chong, Peng[b], Peng Zheng[a], Xilong Wang[a], Jiyuan Fan[a], Jinlin Mei[a], Chunming Xu[a], Aijun Duan[a,*]

[a] State Key Laboratory of Heavy Oil Processing, China University of Petroleum, Beijing, 102249, P. R. China.

[b] Dalian Research Institute of Petroleum and Petrochemicals, SINOPEC, Dalian 116041, Liaoning, China

* Corresponding authors: Aijun Duan, Xia Zhang

E-mail address: duanaijun@cup.edu.cn ; zhangxia.fshy@sinopec.com

Abstract: Dual-metal modifications on SBA-16 silica were implemented to modulate the acidities and the distribution and dispersion of active phases for NiMo catalysts. The results showed that the acidity of S-H groups in S-edge sites can be promoted by B acid and further facilitate the DDS selectivity. The NiMo/AT-7.5 catalyst exhibits the highest HDS efficiency of 97.5% due to its appropriate acidity, highest proportion of MoS_2 phase and concentration of S-edge sites. The kinetic and thermodynamic analyses were applied to investigate the intrinsic HDS reactivity for various catalysts. The results confirmed the existence of synergistic effect in the DBT HDS reaction. The B acid sites can further increase the desulfurization route (DS) of THDBT to CHB. A higher dispersion degree of MoS_2 could improve DBT HDS efficiency. A high total concentration of S-edge and Mo-edge will indicate a high HDS efficiency. The S-edge/Mo-edge ratio and k_{DDS}/k_{HYD} could be correlated.

Key words: acidity, active phase, HDS reaction, S-edge and Mo-edge sites

Introduction

Recently, with the increasingly strict environmental regulations, various novel

supports for hydrogenation catalysts are studied to remove the sulfur in the oil product.[1, 2] For designing good-performance hydrotreating catalysts, it is significant to understand the HDS reaction mechanisms and kinetics of sulfur-containing molecules. According to the structure model proposed by Topsøe, the catalytic active sites of Co-Mo-S are located on the edge of MoS_2 slabs.[3] It was reported that MoS_2 slabs principally including two types of edges: the sulfur-terminated edge (S-edge) and Mo-terminated edge (M-edge). [4] Prins reported that DDS reaction may be likely to occur on the metal edges of the Co-MoS_2 crystallites, and the HYD reaction occurs on the brim sites close to the edges of the MoS_2 plane and Co sites located at the metal edge.[5] Moses et al. report that the HYD and DDS routes could occur on the Mo-edge and S-edge, but the breakage of C-S bond is easier to take place on S-edge sites, which is also considered as the rate limiting step in HDS reaction.[6] Oliviero et al reveal that S-edge is intrinsically more active than Mo-edge due to its activation of adsorbing thiophene reactant for subsequent C-S bond breakage in HDS reaction. The adsorption of H on S-edge is stronger than M-edge.[7] Topsoe et al propose that the S-H groups with high hydrogenolysis activity are mainly associated with S-edge and B acidic sites.[8] Han et al disclose that B acid sites not only can promote the formation of coordinatively unsaturated sites (CUS) sites, but also increase the acidity of -SH sites and further improve the hydrogenolysis activity.[9] Meanwhile, the fully sulfide Mo-edge sites can promote the HYD route.[10]

Besides understanding the effect of different active sites, the supports of hydrotreating catalysts with excellent physico-chemical properties for promoting the dispersion of active metals and reactant diffusion should also be developed. Noticeably, mesoporous materials have been wildly applied in the fields of catalysis, adsorption and separation due to their high pore size, pore volume, surface area and

structural order degree.[11, 12] Among these materials, SBA-16 silica with highly ordered degree possesses large cage-like mesopores arranged in cubic body-centered *Im3m* symmetry, which will lead to lower mass transfer resistance and further facilitate the catalytic reactions.[13] However, SBA-16 pure silica presents low acidity and poor dispersion of active metals, which is adverse to HDS reaction. Therefore, it is necessary to incorporate other atoms into the SBA-16 material for increasing the acidity of catalysts and dispersion of active metals. Typically, Al modification into pure silica materials can strongly improve the amount of acidity.[14] Meanwhile, the incorporation of Ti or Zr atoms into pure silica materials can improve the properties of active metals.[15-18] Mere incorporation of single atoms into SBA-16 pure silica shows advantages and disadvantages. Therefore, it is necessary to incorporate dual metals into SBA-16 materials for obtaining high-efficiency catalysts.

In this study, serial Al-Ti-SBA-16 composites with different acidities and physico-chemical properties were successfully prepared. Before introducing Al species, the Ti-SBA-16 precursors were prepared by a two-step method through pre-hydrolysis of TEOS before the addition of tetrabutyl titanate for protecting the original structure of SBA-16 silica. Various characterization methods were carried out on Al-Ti-SBA-16 composites and corresponding NiMo/Al-Ti-SBA-16 catalysts to investigate the influence of Al and Ti species on their properties. Moreover, the HDS performances of NiMo/SBA-16 and NiMo/Al-Ti-SBA-16 catalysts were also evaluated to correlate the relationship between the HDS activity and selectivity and properties of support and catalysts. An appropriate composition of Al and Ti species in the NiMo/Al-Ti-SBA-16 catalysts, which will allow the highest HDS efficiency, were obtained. The relationship between S-edge and Mo-edge sites and HDS performance and selectivity was also proposed. Finally, the kinetic and thermodynamic analyses

were applied to investigate the influence of S-edge and Mo-edge on the intrinsic HDS reactivity for various catalysts.

Experimental

The preparation methods of materials, characterization methods, catalytic test methods and some calculation methods are all shown in the Support Information.

Kinetic analysis

The HDS reaction of DBT reactant exhibit two types routes of including DDS and HYD route with follow desulfurization (DS), which is presented in Scheme 1. The corresponding products are tetrahydrodibenzothiophene (THDBT), biphenyl (BP) and cyclohexylbenzene (CHB).

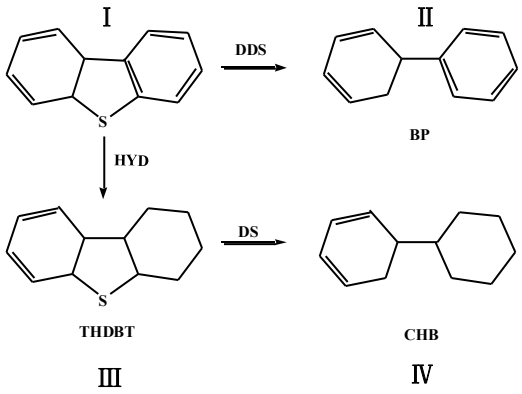

Scheme 1 the DBT HDS reaction routes

HDS reaction for DBT is generally considered as a pseudo-first-order, the HDS rate constant k_{HDS} is obtained by the equation as follows:

$$k_{HDS} = \frac{F}{m} \ln\left(\frac{1}{1-\tau}\right) \quad (4)$$

in which F is the feeding rate of DBT reactant with the unit of mol h^{-1}, m is the mass of loading catalyst with the unit of g, and τ is the conversion of DBT reactant.[19]

The formula system according to the reaction mechanism of Scheme 1 is shown in equation 1 to equation 3, in which c_n and r_n represent the molar concentration of

species n (n= Ⅰ, Ⅱ, Ⅲ and Ⅳ) and the reaction rate. k_i represent the reaction rate constants for each steps in Scheme 1, which include k_{DDS}, k_{HYD} and k_{DS}. The DBT HDS conversions lower than 35% are applied to calculate the above reaction rate constants.

$$r_I = -(k_{HYD}+k_{DDS})\, C_I \quad (5)$$

$$r_{II} = k_{DDS}\, C_I \quad (6)$$

$$r_{III} = k_{HYD}\, C_I - k_{DS} C_{III} \quad (7)$$

$$r_{IV} = k_{DS}\, C_{III} \quad (8)$$

The DBT HDS rate can also be indicated by turnover frequency, TOF (h^{-1}), which is calculated by the following equation:

$$TOF = (F\times\tau) / (n_{Mo}\times f_{Mo}) \quad (9)$$

where n_{Mo} is molar quantity of Mo atoms in the catalysts. τ and f_{Mo} are in consistent with the above definitions.[12]

Moreover, the Arrhenius and Eyring equations could be used to obtain the activation parameters by draw the figures of ln k_{HDS} vs 1/T, and ln(k_{HDS}/T) vs 1/T.[20,21]

$$\ln k_{HDS} = \ln A - (E_a/RT) \quad (10)$$

$$\ln (k_{HDS}/T) = \ln (k_B/h) + (\Delta S/R) - (\Delta H/RT) \quad (11)$$

In the above two equations, Ea is the activation energy with the unit of $kJ\cdot mol^{-1}$, k_B is Boltzmann's constant of 1.381×10^{-23} $J\cdot K^{-1}$, h is Planck's constant of 6.626×10^{-34} $J\cdot s$, ΔS is the activation entropy with the unit of $J\ mol^{-1}\cdot K^{-1}$, ΔH is the activation enthalpy with the unit of $kJ\cdot mol^{-1}$, and R is the ideal gas constant of 8.314 $J\cdot K^{-1}\cdot mol^{-1}$.

Results and discussion

Properties of supports

Small angle XRD patterns of various supports are displayed in Fig. S1. It showed that all samples present a sharp peak ranged from 0.5° to 1°, which is an indicative of (110) reflection and a 3D cubic meso-structure with *Im3m* space group. Meanwhile, a poor-resolved shoulder at about 1.2° should be assigned to (200) reflection.[22] It can deduce that SBA-16 silica is successfully synthesized and the structural order degree of SBA-16 material can be maintained after incorporation of Al and Ti species.

N_2 adsorption–desorption isotherms of different supports are shown in Fig. S2. The textural properties of different supports, determined from N_2 adsorption–desorption isotherms, are displayed in Table 1. The BET surface area and pore volume of SBA-16 pure silica are the highest of 975.7 $m^2 \cdot g^{-1}$ and 1.38 $cm^3 \cdot g^{-1}$, respectively. The pore size of SBA-16 pure silica is lower than that of Al-Ti-SBA-16 composites except AT-0 support, which may be resulted from the longer calcination time for AT-7.5, AT-10, AT-5 and AT-2.5 supports and further generation of intergranular pores. Moreover, the cubic unit cell parameters a_0 of Al-Ti-SBA-16 composites modified by duplex metals are higher than those of SBA-16 pure silica and only Al or Ti modified SBA-16 materials. The mesopores void fractions ε_{mes} of Al-Ti-SBA-16 composites ranged from 0.66 to 0.69 are lower than that of SBA-16 material. The diameter of the spherical cavities D_{me} for AT-2.5 support presents the highest value of 3.80 nm. The wall thickness h_w of Al-Ti-SBA-16 composites composed of both Al and Ti atoms are higher than other materials. Above all, the incorporation of Al and Ti species through the stepwise method can protect the textural properties and maintain the highly ordered degree of SBA-16 silica.

Table 1 Textural properties of serial supports.

Samples	S_{BET} ($m^2 \cdot g^{-1}$)	V_t ($cm^3 \cdot g^{-1}$)	d^a (nm)	$a_0{}^b$ (nm)	$\varepsilon_{mes}{}^c$	$D_{me}{}^d$ (nm)	$h_w{}^e$ (nm)
SBA-16	975.7	1.38	5.67	10.98	0.72	3.56	3.84
AT-10	573.1	1.00	5.73	10.90	0.66	3.23	3.71
AT-7.5	769.6	1.15	5.80	11.17	0.69	3.45	3.88

AT-5	787.8	1.14	5.77	12.26	0.68	3.78	4.85
AT-2.5	766.3	1.14	5.97	12.33	0.68	3.80	4.71
AT-0	792.2	1.02	5.15	10.79	0.66	3.22	4.20

[a] pore size from BET report; [b] cubic unit cell parameter, $a_0=\sqrt{2}d_{110;}$ [c] mesopores void fraction; [d] diameter of the spherical cavities; [e] the wall thickness $h_w=\frac{\sqrt{3}a_0}{2}-d$.

Raman spectra of different supports are displayed in Fig. S3. For SBA-16 and AT-10 support (only modified by Al species), three peaks appearing at 491, 604, and 977 cm^{-1} should be assigned to pure silica.[24] An obvious peak at about 879 cm^{-1} appearing in the spectrum of AT-10 sample should be assigned to the non-spinel γ-Al_2O_3 phase.[25] As reported, two peaks at 491 and 604 cm^{-1} should be ascribed to the tri- and tetracyclosiloxane rings generated by the condensation of surface (–OH) groups. Meanwhile, the band at 977 cm^{-1} is resulted from the surface Si–OH stretching mode.[26] As for the supports modified by Al and Ti species, the peaks assigned to silica and Al_2O_3 become too weak to be observed due to strong intensities of peaks belonging to TiO_2 phase. Four characteristic peaks at 144 cm^{-1} 399, 515 and 634 cm^{-1} observed in the spectra of AT-7.5, AT-5, AT-2.5 and AT-0 samples are ascribed to anatase phase.[27]

The UV–vis DRS spectra of various supports with different compositions are shown in Fig. S4A. All supports exhibit different adsorption bands with the change of addition amount of Ti sources. There are no adsorption bands appearing in AT-10 samples due to Al and Si species are transparent in the UV-vis DRS detected region. The absorption bands in the samples containing Ti species are resulted from the ligand-to-metal charge transfer from the O^{2-} to Ti^{4+} to form its charge-transfer excited state, (Ti^{3+}–O^{-}).[28] For the samples incorporated into Ti atoms, the first peaks in the adsorption range of 200-220 cm^{-1} is ascribed to the charge-transfer transitions of oxygen to tetrahedrally coordinated Ti^{4+} ions in the group of $Ti(OSi)^4$, which can

demonstrate that Ti atoms are successfully incorporated into the framework of SBA-16 materials.[29] The bands ranged from 220 to 230 nm can be observed in AT-5, AT-2.5 and AT-0 samples, which are ascribed to the group of $Ti(OH)–(OSi)_3$ in framework of SBA-16 silica.[30] Meanwhile, obvious absorption bands in the region of 300-330 nm can be observed in samples containing Ti atoms, which can be ascribed to Ti-O-Ti bonds and the titanium sites with high coordination numbers.[31] These results confirm that the Ti species should be co-existed in the framework and external framework as TiO_2 crystal phases in the Al-Ti-SBA-16 composites, which is in accordance with Raman measurements. In addition, band gap energy can be estimated from a plot of $(\alpha)^{1/2}$ versus photon energy (hv). The band gap energy for TiO_2 phases can be obtained by extrapolating the linear part of the rising curve to zero. Higher band gap energy will indicate smaller particle size of TiO_2 crystal inside the Al-Ti-SBA-16 composites. The absorption coefficient α can be calculated from the following equation of $\alpha=2303\rho A/(lcm)$, in which ρ (TiO_2) =3.9 $g\cdot cm^{-3}$, A is the absorption intensity, l is the optical path length, c is the molar concentration for TiO_2 and m is molecular weight of TiO_2.[32] From Fig. S4B, the band gap energies follows in the order of AT-7.5 (3.00 eV) > AT-5 (2.94 eV) > AT-2.5 (2.80 eV) > AT-0 (2.50 eV). Therefore, the particle size of TiO_2 crystal in the samples follows the reverse order and increase with the additional amounts of Ti sources.

^{27}Al NMR was also applied to obtain the existent form for Al species in the Al-Ti-SBA-16 composite. It can be generally recognized that the band appearing at about 6 ppm can be ascribed to the octahedral structural unit AlO_6, which can be treated as extra-framework Al species. The band at about 33 ppm has been ascribed to the extra-framework coordination of Al^{3+} as pentahedral AlO_5 unit. Meanwhile, the chemical shift at about 53 ppm is assigned to tetrahedral structural unit AlO_4, in which

aluminum is covalently connected with four Si atoms through oxygen bridges.[33, 34] The ^{27}Al NMR spectrum of AT-5 support is shown in Fig. S5. It presents three peaks belonging to AlO_4, AlO_5 and AlO_6 structural units, indicating that the composites synthesized by this two-step method possess different Al species in framework and extra-framework.

The XPS spectra for different supports are shown in Fig. S6. Ti 2p envelop shows two characteristic peaks at about 485 and 464 eV, being ascribed to Ti 2p3/2 and Ti 2p1/2 species, which is in accordance with the reported literature.[35] It is obvious that the intensity of the above two peaks increase with the Ti contents in the supports. This result can confirm the appearance of TiO_2 phase on the surface of support, which can be seen in Raman and XRD results. From Al 2p XPS envelop, it can also be seen that the intensity of the characteristic peak increase with the Al contents in the supports, which is similar with that of Ti 2p XPS spectra. As shown in O1s XPS envelop, an obvious peak at 533.0 eV can be assigned to the Si-O-Si bond. As the composition of Ti species reaches 10%, a weak peak at about 529 eV can be observed, which should be assigned to the oxygen in the Ti-O-Si bond.[35, 36] This may demonstrate that Ti atoms have been successfully incorporated into the framework of SBA-16 material. The binding energy of AT-10 sample shifting to lower values compared with SBA-16 sample may be caused by the Al incorporation of Al atoms into SBA-16 material, which can be verified from ^{27}Al NMR result. All Si 2p XPS spectra show intensive peaks in the region ranged from 100 to 105 eV. For the spectra of supports containing Al atoms, the bands at about 101 eV, and 103 eV should be ascribed to the bonds of Si-O-Al and Si-O-Si respectively.[37] The binding energy of bands assigned to the Ti-O-Si bond is lower than that of SiO_2.[38] The Si 2p XPS spectra exhibit that the binding energies of Al-Ti-SBA-16 composites shift to lower values compared with

SBA-16 silica, which should be due to the incorporation of Al and Ti species into SBA-16 materials.

The SEM images of different supports are shown in Fig. S7. The SBA-16 pure silica presents regular particles with the morphology of cross-linked sphere. The AT-0 sample modified by Al species through the post-synthetic method exhibits a similar morphology with SBA-16 silica. Compared with SBA-16 and AT-10 samples, the AT-7.5, AT-5 and AT-2.5 samples exhibit different morphologies with relatively lower regularity, which should be caused by the addition of Ti sources. However, particles with the shape of inerratic polyhedron can be observed in AT-0 sample. In addition, the SEM mapping result of AT-5 sample is presented in the Fig. S8. It can be seen that the Al and Ti atoms dispersed well in the surface of AT-5 composite. The SEM EDS results of AT-0 and AT-5 samples are displayed in Fig. S9. The Al composition in AT-0 sample is detected as 11.4%, and Al and Ti compositions in the AT-5 sample are 6.4% and 5.1%, which are similar with theoretical value of Al and Ti compositions. Hence, it can further confirm that the stepwise synthetic method is effective to obtain serial Al-Ti-SBA-16 composites.

The TEM images of SBA-16 and Al-Ti-SBA-16 materials are displayed in Fig. S10. The (111) or (100) crystal faces with highly ordered degree can be clearly observed in all supports. Accompanied with small angel XRD results, the TEM measurements can also demonstrate that serial SBA-16 silica and Al-Ti-SBA-16 materials possesses highly ordered cubic body-centred Im3m symmetry structure.[22]

Properties of catalysts

Raman spectroscopy is an effective measurement to obtain the existent form of the crystalline and amorphous oxides.[39] The Raman spectra of oxidic NiMo/SBA-16 and NiMo/Al-Ti-SBA-16 catalysts are presented in Fig. S11. As reported, the

characteristic peaks in the region of 750-1000 cm^{-1} can be ascribed to Mo oxide species.[40] Four peaks appearing at about 825, 898, 945 and 954 cm^{-1} can be observed in the Raman spectra for all catalysts. The appearance of peak at 825 cm^{-1} should be due to Mo-O-Mo linkage in the polymerized Mo oxide species (orthorhombic MoO_3).[41] The peak at about 898 cm^{-1} should be ascribed to the highly dispersed Mo species, which is tetrahedral coordinated and denoted as Mo(Td).[42] The intensities of the peak at 898 cm^{-1} present a decreasing tendency with the Al compositions in NiMo/Al-Ti-SBA-16 catalysts. Therefore, incorporation of Al species into SBA-16 material can increase the proportion of Mo(Td) species on NiMo loading catalysts. Moreover, the couple peaks at about 945 and 954 cm^{-1} should be assigned to octahedrally coordinated Mo oxide species, Mo(Oh) and $Mo_8O_{26}^{4-}$ species respectively. Noticeably, the Mo(Oh) species are considered as the active phase for HDS reaction, due to the weak interaction between Mo(Oh) species and supports and a higher reducibility and efficiency in HDS reaction.[42] For NiMo/SBA-16 catalyst, the peak at about 981 cm^{-1} can be attributed to symmetric stretching vibration of surface dioxo species $Mo(=O)_2$. No peaks appearing in 990-1000 cm^{-1} prove that the Mo species dispersed well on the surface of serial catalysts.[43]

H_2-TPR measurements were detected for investigating the influences of Al and Ti modification on the reducibility of active metals and the interactions between metals and supports. H_2-TPR profiles of different oxidic NiMo catalysts are shown in Fig. S12. All profiles present a broad reduction band with two peaks ranging from 350 °C to 750 °C. The first peak at low temperature in the ranges of 430-480 °C can be ascribed to the reduction step of octahedrally coordinated Ni^{2+} species in contact with molybdenum.[43] The second peak at high temperature from 530°C to 580°C can be assigned to the reduction of Mo^{6+} to Mo^{4+} for octahedral Mo species, Mo (Oh) and

also $NiMoO_4$ phase.[44] The peak at about 616 °C appearing in NiMo/AT-2.5 catalyst should be assigned to the reduction of bulk MoO_3.[45] The two reduction peaks of NiMo/AT-10 catalyst shift to higher temperatures compared with NiMo/SBA-16 catalyst. Therefore, the interaction strength between metals and support (MSI) for NiMo/AT-10 catalyst is higher than that of NiMo/SBA-16 catalyst. It should be noteworthy that positions of the first peaks for NiMo/AT-7.5, NiMo/AT-5, NiMo/AT-2.5, NiMo/AT-0 catalysts exhibit a decreasing tendency with the Ti additional amounts, which are also lower than those of NiMo/AT-10 and NiMo/SBA-16 catalysts. Therefore, Ti modification can promote the reducibility of octahedrally coordinated Ni and Mo species. However, after Ti modification, the shift of second reduction peaks to higher temperatures may be due to larger amount of Mo (Oh) species in NiMo catalyst with the increasing Ti composition, which is also indicative of the stronger interaction strength between Mo (Oh) phase and support.

UV-vis DRS spectra of oxidic NiMo loading catalysts with different Al and Ti compositions were detected for getting more information about the coordination of oxidic Ni and Mo species. As shown in Fig. S13, the broad absorption bands in the ranges of 200−400 nm appearing in all catalysts should be ascribed to the charge transfer of O^{2-} to Mo^{6+}. The exact position in this characteristic band reflects the state of oxidic Mo species. The absorption band ranged from 200 to 280 nm can be ascribed to tetrahedral Mo species, Mo (TD) with highly dispersion degree. Meanwhile, the adsorption band in the region of 280-400 nm is assigned to octahedral Mo species, Mo (Oh).[46] Compared with NiMo/SBA-16 catalyst, the bands in the ranges of 280-400nm for NiMo/AT-10 catalyst shows a blue shift, indicating an increasing proportion of Mo (Td) species, which is consistent with the result of Raman measurements. Meanwhile, with the increasing amount of Ti species in the

catalysts, the bands in the ranges of 280-400nm exhibit a red shift to higher wavelength, demonstrating that the incorporation of Ti atoms into SBA-16 material can increase the proportion of Mo (Oh) species.

Table 2 Acid properties for different NiMo catalysts, which is determined by the above FT-IR pyridine spectra.

Catalysts	Acid amount (200 ºC)/μmol·g^{-1}				Acid amount (350 ºC)/μmol·g^{-1}			
	B	L	B+L	B/L	B	L	B+L	B/L
NiMo/SBA-16	20.9	31.1	52.0	0.67	0.0	3.3	3.3	0
NiMo/AT-10	28.2	113.5	141.7	0.25	24.2	56.7	80.9	0.43
NiMo/AT-7.5	26.7	83.7	110.4	0.32	18.3	31.5	49.80	0.58
NiMo/AT-5	24.5	80.0	104.5	0.31	17.1	30.3	47.40	0.56
NiMo/AT-2.5	22.4	50.1	72.5	0.45	11.3	26.3	37.60	0.43
NiMo/AT-0	21.9	47.4	69.3	0.46	0.0	5.7	5.70	0

FT-IR pyridine spectroscopy has been applied to obtain the surface acid amount of various catalysts. The FT-IR pyridine spectra recorded at two adsorption temperatures of 200 °C and 350 °C are displayed in Fig. S14. As reported, the peak appearing at 1540 cm^{-1} can be ascribed to the Brönsted acid sites (B). The peak at about 1490 cm^{-1} is resulted from both Brönsted and Lewis acid sites. Two characteristic peaks at 1450 cm^{-1} and 1610 cm^{-1} can be ascribed to Lewis acid sites (L).[47] In addition, a shoulder at about 1620 cm^{-1} appeared in the patterns of the NiMo catalysts containing Al species can be assigned to Lewis acid sites,[48] which may be caused by exposed Al^{3+} ions. It should be noteworthy that the intensity of peaks belonging to B and L acid sites increase after Al and Ti modification. Therefore, it can deduce that the incorporation of Al and Ti atoms into SBA-16 material can increase the amount of B acid sites and L acid sites. The amounts of Brönsted, Lewis, total acid sites and the B/L ratios determined from Fig. S14 are concluded in Table 2. The adsorption intensity of pyridine molecules degassed at 200 °C and 350 °C on the surface of NiMo catalysts should be ascribed to the amount of total acid sites and the amounts of medium and strong acid sites, respectively.[14] From Table 2, the amounts of B acid

sites, L acid sites and B+L acid sites for other catalysts increase after Al and Ti modification. The total amounts and the amounts of medium and strong acid sites follow the order of NiMo/SBA-16 < NiMo/AT-0 < NiMo/AT-2.5 < NiMo/AT-5 <NiMo/AT-7.5 <NiMo/AT-10. Therefore, incorporation of Al species into SBA-16 materials can generate more acid sites than those of Ti species. Moreover, the B/L ratio for NiMo/SBA-16 catalyst is higher than those of NiMo/Al-Ti-SBA-16 catalysts, indicating that Al and Ti modification can generate more L acid sites than B acid sites. For NiMo/SBA-16 and NiMo/AT-0 catalysts, the amount of medium and strong acid sites of B type are 0 $\mu mol \cdot g^{-1}$, confirming that the incorporation of Ti atoms into SBA-16 material can mainly generate L type acid sites by Ti species appending to the support through surface silanol groups.[49]

Table 3 the proportion of Mo species over different sulfide catalysts, as determined by XPS spectra.

Catalyst	Mo^{4+}/Mo_{total}	Mo^{5+}/Mo_{total}	Mo^{6+}/Mo_{total}	Ni/Si	Mo/Si
NiMo/SBA-16	0.30	0.09	0.61	0.017	0.037
NiMo/AT-10	0.50	0.12	0.38	0.020	0.039
NiMo/AT-7.5	0.56	0.12	0.32	0.023	0.046
NiMo/AT-5	0.52	0.25	0.23	0.025	0.048
NiMo/AT-2.5	0.53	0.22	0.25	0.029	0.051
NiMo/AT-0	0.54	0.26	0.20	0.022	0.041

To study the proportions of active metals over the surface of different NiMo sulfide catalysts, XPS spectroscopy were detected. The XPS patterns of Mo3d in the ranges of 220-242 eV is displayed in Fig. S15. As reported, the binding energies for sulfide Mo 3d5/2 species, including $Mo^{6+}(MoO_3)$, Mo^{5+}(oxysulfide), $Mo^{4+}(MoS_2)$, are 232.3±0.3 eV, 228.6±0.3 eV, 230.7±0.3 eV, respectively. Moreover, the peak at 226.0 ± 0.3 eV can be corresponding to S2s. [21] The positions of peaks assigned to Mo

3d3/2 species are fixed at adding 3.1 eV on the basis of those of Mo 3d5/2 species. The area ratios of Mo 3d5/2 and the Mo 3d3/2 species are fixed at 1.5. The half peak widths for all sulfide catalysts are same. Meanwhile, the corresponding data of the fitted peaks for Mo species are shown in Table 3. The Mo^{4+}(MoS_2) species are generally treated as active phase for HDS reaction. The proportions of Mo^{4+} species over various catalysts follow in the sequence of NiMo/SBA-16 (0.30) < NiMo/AT-10 (0.45) < NiMo/AT-7.5 (0.56) < NiMo/AT-5 (0.52) < NiMo/AT-2.5 (0.54) < NiMo/AT-0 (0.53). Therefore, Al and Ti modification can significantly increase the proportion of MoS_2 species. As the Al and Ti compositions are 7.5% and 2.5%, the NiMo/AT-7.5 exhibit the highest proportion of Mo^{4+}(MoS_2). Hence, the incorporation of Ti species can also facilitate the formation of MoS_2 active phases, which is in accordance with the literature.[50] Moreover, Ni/Si and Mo/Si ratios on the surface of serial NiMo/AT-SBA-16 catalysts, which can reflect the dispersion degree of Ni and Mo active metals, were higher than those of NiMo/SBA-16. Therefore, Al and Ti modification can improve the dispersion degree of active metals, which may allow a high HDS efficiency.

Table 4 The distributions of the Ni species for different sulfide catalysts, as derived from XPS analysis.

Catalysts	NiS/Ni_T	NiO/Ni_T	$NiMoS/Ni_T$
NiMo/SBA-16	0.49	0.25	0.25
NiMo/AT-10	0.47	0.25	0.28
NiMo/AT-7.5	0.34	0.25	0.41
NiMo/AT-5	0.36	0.26	0.38
NiMo/AT-2.5	0.34	0.24	0.42
NiMo/AT-0	0.39	0.24	0.37

The Ni 2p XPS spectra of different sulfide catalysts are shown in Fig. S16. Meanwhile, the peak-fitting data for Ni 2p species are displayed in Table 4. The Ni

species in XPS spectra include three kinds of NiMoS, NiS and NiO.[51] The binding energy for NiMoS active phase appears at 856.0±0.3 eV. The binding energies for Ni 2p1/2 and NiS 2p3/2 are 873.0±0.3 eV and 852.6±0.3 eV respectively. Moreover, the binding energy appearing at 862.0±0.3 eV is ascribed to NiO species.[52] It reveals that the proportion of NiMoS phase exhibit the order of NiMo/SBA-16 (0.25) < NiMo/AT-10 (0.28) < NiMo/AT-0 (0.37) < NiMo/AT-5 (0.38) < NiMo/AT-7.5 (0.41) < NiMo/AT-2.5 (0.42). The proportion of NiMoS phase for the sulfide catalysts incorporated by Al or Ti species, particularly Ti species is higher than that of NiMo/SBA-16 catalyst. Therefore, it can demonstrate that appropriate Ti modification can promote the distribution of active metals, which can also be recognized from UV-vis DRS. It should be noteworthy that the NiMoS phase is generally treated as active phase for HDS reaction. Hence, the incorporation of Ti species into SBA-16 silica can improve the HDS performance through improving the distribution of active metals.

Table 5 Mo edge and S edge concentration from CO-IR spectra.

Catalysts	S-edge concentration (μmol/g)	Mo-edge concentration (μmol/g)	Total edge concentration (μmol/g)	S-edge/Mo-edge
NiMo/SBA-16	4.60	38.38	42.98	0.12
NiMo/AT-10	8.12	47.41	55.53	0.17
NiMo/AT-7.5	9.70	60.42	70.12	0.16
NiMo/AT-5	7.30	65.73	73.03	0.11
NiMo/AT-2.5	6.38	69.00	75.38	0.09
NiMo/AT-0	4.90	58.58	63.48	0.08

CO-IR spectra were applied to investigate the concentration of active metals over serial sulfide NiMo catalysts, which were shown in Fig. S17. It is well investigated that MoS_2 slabs possess two types of edges including the sulfur-terminated edge (S-edge) and Mo-terminated edge (Mo-edge).[53] Because the sample are detected without H_2 treatment, the symmetrical band at about 2105 cm^{-1} assigned to CO

adsorption on the Mo-edge sites with a high sulfur coordination number can be observed, which is also considered as fully sulfide species.[54] Three bands at 2065 cm^{-1}, 2045 cm^{-1} and 2020 cm^{-1} signify the existence of CO adsorbed on the S-edge with different sulfur coverage.[7,56] The band at about 2130 cm^{-1} should be assigned to partial sulfided MoOxSy phase or NiMoS phase.[55,56] The band appears at 2156 cm^{-1} is due to CO adsorbed on surface OH group.[55] The decomposition data of CO-IR spectra were concluded in Table 5. As the addictive amounts of metals are same, a higher total concentration of Mo-edge and S-edge will indicate a better dispersion of active metals. It shows that the total concentrations of Mo-edge and S-edge increase after Al and Ti modification, which follows the sequence of NiMo/SBA-16 < NiMo/AT-10 < NiMo/AT-0 < NiMo/AT-7.5 < NiMo/AT-5 < NiMo/AT-2.5, demonstrating that the incorporation of Al and Ti species into SBA-16 material can enhance the dispersion degree of metals. The total concentration of Mo-edge and S-edge for NiMo/AT-10 catalyst is lower than NiMo/AT-0 catalyst, verifying that Ti modification can improve higher dispersion degree of active metal than that of Al modification. However, as the mass percentage of TiO_2 in support reaches 10%, the total concentration for NiMo/AT-0 catalyst is lower than other catalysts containing both Al and Ti species. It should be noteworthy that the concentration of S-edge exhibits an increasing trend with the Al contents in supports, peaking at 9.70 μmol/g for NiMo/AT-7.5 catalyst. Hence, incorporation of Al species into SBA-16 silica can promote the formation of S-edge. In order to acknowledge the influence of acidity on the formation of S-edge sites, the plots of amount of B acid sites and the concentration of S-edge are shown in Fig. S18. It shows that the S-edge concentration presents an increasing tendency with the amounts of B acid, indicating that the B acid sites can facilitate the formation of S-edge sites. However, the lower concentration of S-edge

for NiMo/AT-10 catalyst than NiMo/AT-7.5 catalyst should be assigned to its lower dispersion degree f_{Mo} of MoS_2, which can be recognized from HRTEM results. Moreover, the concentration of fully sulfide Mo-edge sites over sulfide NiMo catalysts exhibit an increasing trend with the contents of Ti species. As the TiO_2 content reaches 10% in support, the concentration of Mo-edge site becomes lower than other catalysts containing Ti species, which may be also related to its relatively low dispersion degree of active metals. In addition, the ratios of S-edge and Mo-edge are also calculated and exhibit an increasing trend with the contents of Al species.

HRTEM measurement was applied for obtaining the dispersion information of active phase MoS_2. The representative images of different sulfide catalysts are displayed in Fig. S19. The stacking-number distributions of MoS_2 crystallines for serial sulfide catalysts are exhibited in Fig. S20. It is obvious that the proportion of MoS_2 phases with lower stacking layers, especially the 2 layers, show an increasing tendency with the Al and Ti compositions in the catalysts. It can be verified from H_2-TPR result that the interaction strength between active Mo (Oh) phase and support become stronger after Al and Ti modification, which will lead to the decrement of stacking layers of MoS_2. Fig. S21 exhibits that the frequency of MoS_2 phases with short slab length ranging from 0-2 nm and 2-4 nm increases after Al and Ti modification. Whereas, the frequency of MoS_2 with higher slab length present the reverse trend. Moreover, the average length and number of slabs and dispersion degree (f_{Mo}) for MoS_2 slabs are displayed in Table S1. As compared with NiMo/SBA-16 catalyst, the average length and stacking layers of various NiMo/Al-Ti-SBA-16 catalysts are relatively lower. The dispersion degree of MoS_2 phase over sulfide NiMo/Al-Ti-SBA-16 is improved after the incorporation of Al and Ti species into SBA-16 materials, which follows the order of NiMo/SBA-16 (0.14) <

NiMo/AT-10 (0.16) < NiMo/AT-0 (0.18) < NiMo/AT-7.5 (0.20) < NiMo/AT-5 (0.21) < NiMo/AT-2.5 (0.23). Above all, sulfide NiMo/SBA-16 catalyst presents the highest slab numbers, longest slab length and lowest dispersion degree, which are adverse for HDS reaction. Al and Ti modification can make an improvement of properties for active metals and further enhance the HDS efficiency for the corresponding catalysts. However, the NiMo/AT-0 catalyst exhibits relatively lower dispersion degree of MoS_2, which may be caused by the fact that the pore size of AT-0 support is the lowest from the above BET result.

Catalytic performance and kinetic analysis

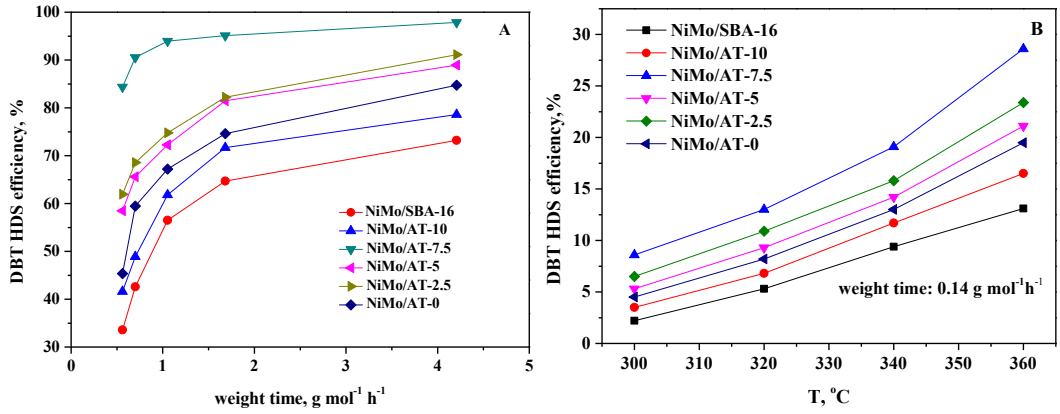

Fig. 1 DBT HDS efficiencies of serial NiMo catalysts under different weight time and reaction temperatures.

The HDS performances of serial NiMo catalysts over DBT reactant at different weight time and reaction temperatures are displayed in Fig. 1. It shows that the HDS performance follows the order of NiMo/SBA-16 < NiMo/AT-10 < NiMo/AT-0 < NiMo/AT-5 < NiMo/AT-2.5 < NiMo/AT-7.5. This result can verify that Al and Ti cooperative modification can significantly improve the HDS performance, which should be ascribed to the fact that the incorporation of Al and Ti atoms into SBA-16 silica can improve the acidity of catalyst and the properties of active metals including dispersion degree and distribution. Although the total amount of acidity of

NiMo/AT-10 is the highest, NiMo/AT-0 catalyst presents a better HDS performance than that of NiMo/AT-10 catalyst, which should be due to its higher proportion of MoS_2 and NiMoS phases (XPS results) and better dispersion for MoS_2 phases (HRTEM results). The NiMo/AT-7.5 catalyst shows the highest HDS efficiency of 97.8% under the reaction conditions of T=340 °C, P=4.0 MPa and WHSV=20 h^{-1}. The HDS efficiency can be correlated to the factors of physico-chemical properties of supports, acidities of catalysts, dispersion and distributions of active metals. The reasons for the highest HDS performance for NiMo/AT-7.5 catalyst should be ascribed to the following factors. The pore volume and pore size of AT-7.5 support are relatively high, and the acidity of corresponding NiMo/AT-7.5 catalyst is appropriate. The XPS results disclose that the proportion of active MoS_2 phase in sulfide NiMo/AT-7.5 catalyst is the highest of 0.56, and the proportion of active NiMoS phase is 0.41, which is only lower than that of sulfide NiMo/AT-2.5 catalyst. Finally, from HRTEM results, the slab length of MoS_2 is short and the dispersion degree of MoS_2 (f_{Mo}) is high. Above all, the synergistic effect of the incorporation by Al and Ti species can enhance the HDS efficiency. In addition, NiMo/AT-2.5 catalyst also exhibit high HDS performance, which may be due to its highest pore size, shortest slab length of 4.0 nm and the highest f_{Mo} value of 0.22. However, the HDS efficiency of NiMo/AT-2.5 catalyst is lower than that of NiMo/AT-7.5 catalyst due to its poor acidic properties.

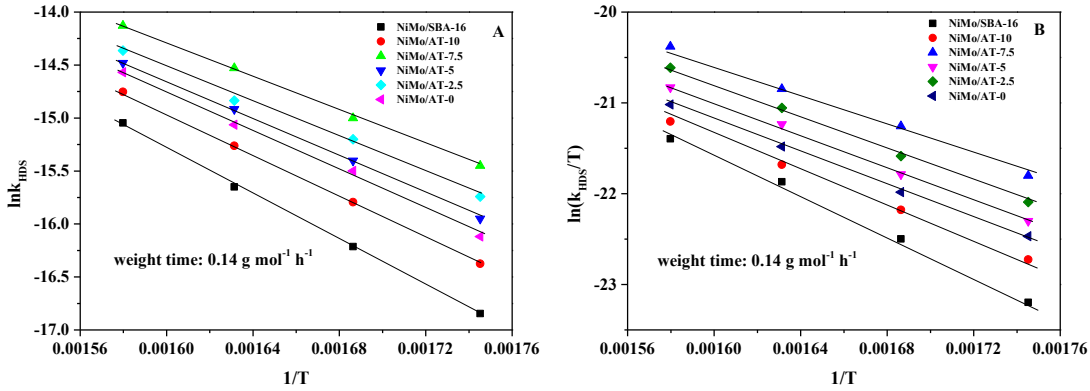

Fig. 2 Arrhenius plots (A) and Eyring plots (B) for DBT HDS reaction on various catalysts.

Table 6 the active energy and thermodynamic parameters over different catalysts for DBT HDS reaction, which are obtained from Arrhenius plots and Eyring plots.

Catalyst	Ea (kJ/mol)	ΔH (kJ/mol)	ΔS (J mol/k)
NiMo/SBA-16	90.7	85.7	-240.8
NiMo/AT-10	81.7	76.7	-252.6
NiMo/AT-7.5	63.5	59.5	-274.6
NiMo/AT-5	74.1	69.1	-262.4
NiMo/AT-2.5	69.4	64.4	-268.8
NiMo/AT-0	78.1	73.1	-256.1

The Arrhenius plots and Eyring plots for various catalysts at the DBT HDS conversion lower than 30% are shown in Fig. 2. The active energies Ea are calculated by the Calculation 10 based on the slopes of the Arrhenius plots. The thermodynamic parameters including enthalpy changes (ΔH) and entropy changes (ΔS) are calculated according to the slopes and intercept of the linear Eyring plots respectively. The above three parameters are concluded in the Table 6. It shows that the values of Ea follow the sequence: NiMo/SBA-16 > NiMo/AT-10 > NiMo/AT-0 > NiMo/AT-5 > NiMo/AT-2.5 > NiMo/AT-7.5. It is well recognized that the higher active energy Ea is, the lower HDS efficiency is. The trend of Ea values can be related with the HDS efficiencies over various catalysts from Fig. 1. Meanwhile, the enthalpy changes (ΔH) and entropy changes (ΔS) for various catalysts exhibit the same increasing order of NiMo/AT-7.5 < NiMo/AT-2.5 < NiMo/AT-5 < NiMo/AT-0 < NiMo/AT-10 <

NiMo/SBA-16. It should also be noteworthy that the lower activation enthalpy value will lead to a more rapid reaction rate for DBT HDS reaction. Therefore, the kinetic and thermodynamic studies demonstrate that NiMo/AT-x catalysts present better HDS performance than NiMo/SBA-16 due to the improvement of acidity and dispersion and distribution of active phases.

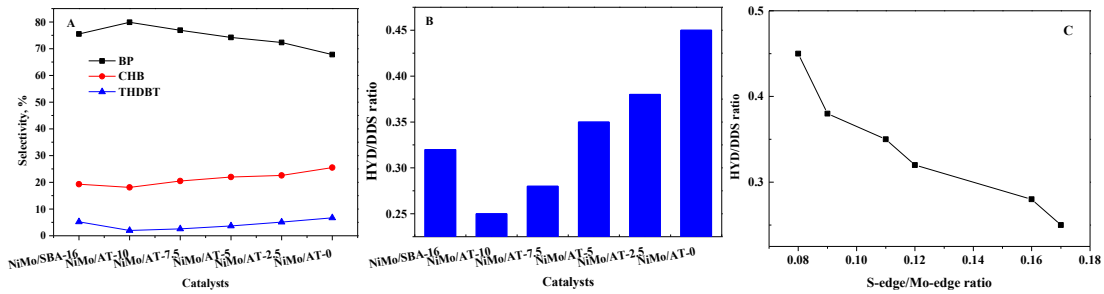

Fig. 3 (A) the product distributions of DBT HDS reaction; (B) the HYD/DDS ratios for various catalysts; (C) the correlation between S-edge/Mo-edge ratio and HYD/DDS ratio.

DBT HDS reaction includes HYD and DDS routes, whose corresponding products are tetrahydrodibenzothiophene (THDBT), biphenyl (BP) and cyclohexylbenzene (CHB). The distributions of DBT HDS reaction routes for serial NiMo catalysts are displayed in Fig. 3A. It can be seen that DDS route should the primary path in DBT HDS reaction due to the HYD and DDS ratios are lower than 1.0. From Fig. 3B, the HYD and DDS ratios follows the order of NiMo/AT-10 < NiMo/AT-7.5 < NiMo/AT-5 < NiMo/SBA-16 < NiMo/AT-2.5 < NiMo/AT-0. The distribution of HDS route can be related with the acidity of catalyst. Compared with NiMo/SBA-16 catalyst, the selectivity of DDS routes for NiMo catalysts containing Al species are enhanced, which should be due to the fact that B acid site can promote the formation of coordinatively unsaturated sites (CUS) by accepting an electron from MoS_2 active phase.[9] NiMo/AT-10 catalyst presents the lowest HYD and DDS ratio of 0.25. In addition, the HYD and DDS ratio for NiMo/AT-0 catalyst is the highest of 0.45,

verifying that the incorporation of Ti atoms into SBA-16 structure can improve the selectivity of HYD route. The improvement of HYD selectivity after Ti modification should be assigned to the special structure and electronic properties of active phases formed on surface of catalyst.[57] Meanwhile, CO-IR results can also disclose the correlation between HDS route and types of active metals.[6] It is recognized that vacant (CUS) sites are responsible for S removal through DDS route, whereas the HYD pathway should be enhanced by a fully sulfide MoS_2 phase.[58] Caused the Mo-edge and S-edge sites play different roles in HDS reaction route, the improvement of DDS route must be at the expanse of HYD route. Therefore, the concentration ratio of S-edge and Mo-edge may be applied to correlate with the HDS selectivity. The relationship between S-edge/Mo-edge ratio and HYD/DDS ratio is shown in Fig. 3C. It shows that the HYD/DDS ratio decreases with the increasing S-edge/Mo-edge ratio. Therefore, the HYD/DDS ratios can be well linked with the S-edge/Mo-edge ratios.

Table 7 the pseudo-first-order constants (10^{-4} mol g^{-1} h^{-1}) and TOF (h^{-1}) of DBT HDS reaction routes for serial NiMo catalysts, which are obtained at the HDS conversions lower than 30%.

Catalyst	k_{DDS}	k_{HYD}	k_{DS}	k_{HDS}	k_{DDS}/k_{HYD}	TOF
NiMo/SBA-16	4.8	1.4	638	6.2	3.5	5.1
NiMo/AT-10	7.4	1.2	1697	8.6	6.2	6.1
NiMo/AT-7.5	13.1	3.2	2080	16.3	4.1	9.0
NiMo/AT-5	8.6	2.6	1579	11.2	3.3	6.9
NiMo/AT-2.5	9.8	3.3	1316	13.1	3.0	7.2
NiMo/AT-0	7.0	3.2	862	10.2	2.2	6.4

The HDS rate constants k_{HDS}, k_{HYD}, k_{DS}, k_{DDS}, k_{DDS}/k_{HYD} and TOF values are provided in Table 7. The values of k_{HYD}, k_{DS} and k_{DDS} kinetic parameters could reflect the reactivity of each reaction steps. k_{DDS}/k_{HYD} may be applied to investigate the HDS selectivity. It shows that the k_{HYD} and k_{DDS} present an increasing tendency with the Ti and Al contents in the NiMo catalysts, demonstrating that incorporation of Ti and Al

into SBA-16 silica can enhance the selectivity of HYD route and DDS route respectively. Noticeably, the k_{DS} value presents an increasing tendency with the amount of B acidity for various catalysts. The NiMo/AT-7.5 exhibits the highest k_{DS} value of 2080 10^{-4} mol g^{-1} h^{-1} may be due to its relative high amount of acidity and the highest amount of S-edge sites.

The k_{HDS} and TOF values could be applied to investigate the intrinsic reactivity of DBT HDS reaction. The k_{HDS} values for serial catalysts present the same tendency with their HDS efficiencies from Fig. 1, confirming that the enhancement of acidity and properties of active phases could improve the DBT HDS performance. NiMo/SBA-16 catalyst shows the lowest k_{HDS} and TOF values of 6.2×10^{-4} mol g^{-1} h^{-1} and 5.1 h^{-1}, and NiMo/AT-7.5 catalyst presents the highest k_{HDS} and TOF values of 16.3×10^{-4} mol g^{-1} h^{-1} and 9.0 h^{-1} respectively. It is wildly accepted that larger amount of vacant sites for active metals will allow a better HDS performance.[59] However, Vogelaar proposed that the fully sulfide catalyst with the lowest amount of CUS sites presents the best HDS performance for thiophene reactant.[54] Combining the CO-IR results and HDS activity, our results show that the HDS efficiencies are mostly linked with the total concentrations of Mo-edge and S-edge, but the NiMo/AT-7.5 exhibit the highest HDS performance even though its total concentration of Mo-edge and S-edge is not the highest. This phenomenon should be correlated with the special properties of -SH groups in S-edge. The acidity of S-edge sites can be enhanced through easily accepting the H^+ from B acid site, which can significantly enhance the DDS route of HDS reaction. Meanwhile, the -SH groups can also act as the H_2 source during the HDS reaction.[8] For NiMo/AT-7.5 catalyst, the S-edge concentration promoted by Al modification is the highest, and the concentration of fully sulfide Mo-edge sites promoted by Ti modification is relatively high. Therefore, the highest k_{HDS} and TOF

values for NiMo/AT-7.5 catalyst can be ascribed to the synergistic effect of the enhancing acidity and distribution and dispersion of active metals. Above all, it can conclude that incorporating appropriate contents of Al and Ti atoms into SBA-16 silica can maximize HDS performance for the corresponding NiMo/Al-Ti-SBA-16 catalyst. The principle is shown in Scheme 2.

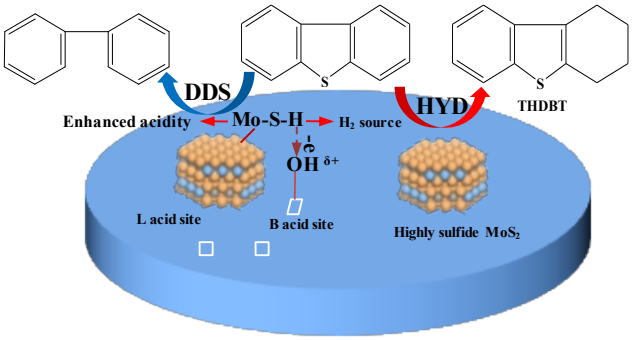

Scheme 2 synergistic effect of Mo-edge and S-edge in HDS reaction for NiMo/Al-Ti-SBA-16 catalysts.

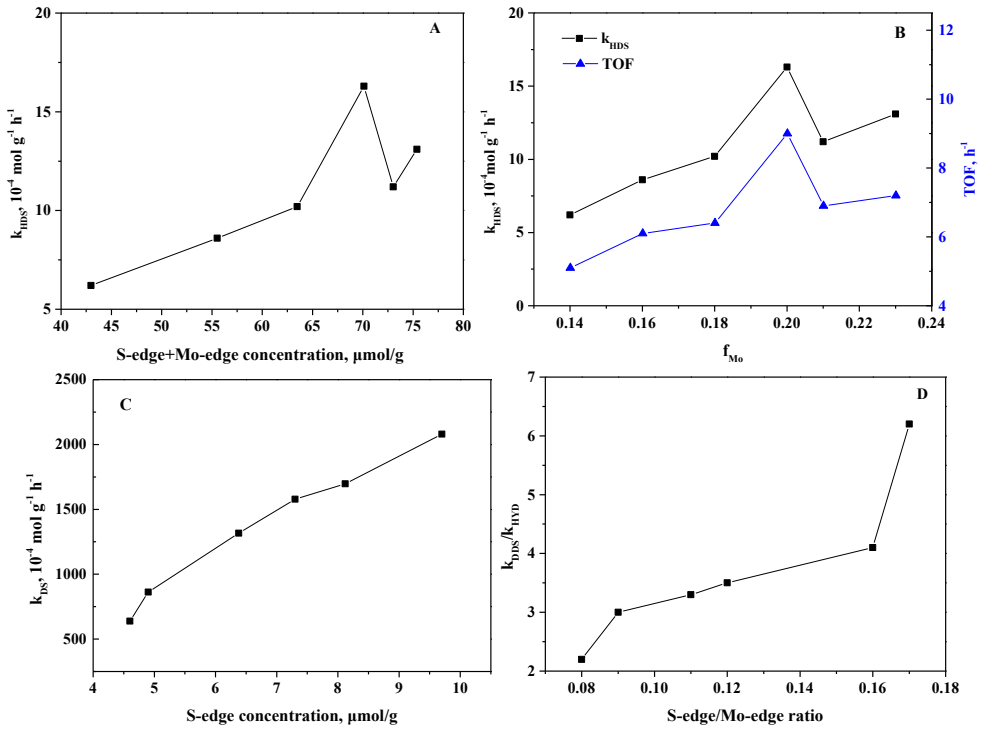

Fig. 4 (A) the correlation between S-edge and Mo-edge concentration and k_{HDS}; (B) the correlation between f_{Mo} and k_{HDS}; (C) the correlation between S-edge concentration and k_{DS}; (D) the correlation between S-edge/Mo-edge ratio and

k_{DDS}/k_{HYD} ratio.

As reported, the dispersion degree of active phases, the concentration of S-edge and Mo-edge sites plays an important role in the HDS reaction.[7,21] The correlations between S-edge and Mo-edge concentration and k_{HDS}, f_{Mo} and k_{HDS}, S-edge concentration and k_{DS} and S-edge/Mo-edge ratio and k_{DDS}/k_{HYD} ratio are concluded in Fig. 4. Fig. 4A and Fig. 4B disclose that the higher MoS_2 dispersion degree (f_{Mo}) and total concentration of S-edge and Mo-edge will allow a higher DBT HDS conversion. The correlation between k_{DS} and S-edge concentration are presented in Fig. 4C. As mentioned before, the S-edge site can facilitate the selectivity of DDS route in DBT HDS reaction. Similarly, the result exhibits that the S-edge site can also facilitate the DS route of THDBT to CHB. From Fig. 4D, higher S-edge/Mo-edge ratio will indicate a higher k_{DDS}/k_{HYD} value, confirming that the S-edge/Mo-edge ratio could be well linked with the HDS selectivity.

Conclusion

Serial Al and Ti modified supports are successfully prepared by a stepwise and post-synthetic method. It is found that the intact structure of SBA-16 material can be maintained after modification of Al and Ti species, whose existent forms in Al-Ti-SBA-16 composite should be co-existed in the framework and external framework. Meanwhile, the incorporation of Al and Ti atoms into SBA-16 material can increase the proportions of Mo(Td) and Mo(Oh) species on NiMo loading catalysts, respectively. The DBT HDS evaluation reveals that the HDS efficiency can be significantly improved by incorporation Al and Ti atoms into NiMo catalysts through enhancing acidity and properties of active metals. NiMo/AT-7.5 catalyst presents the highest HDS efficiency should be ascribed to the factors including high pore volume and pore size of AT-7.5 support, appropriate acidity for NiMo/AT-7.5

catalyst, highest proportion of MoS_2 phase and concentration of S-edge sites with high efficiency. Interestingly, the B acid site can facilitate the formation of S-edge sites. The HYD/DDS ratios can be well related with the concentration ratios of S-edge and Mo-edge. The reason why NiMo/Al-Ti-SBA-16 catalyst shows high HDS performance should be assigned to the synergistic effect with high efficiency. Finally, the kinetic and thermodynamic analyses disclosed that there are correlations existing between amount of B acid sites and k_{DS}, the dispersion degree of MoS_2 and HDS efficiency, the total concentration of S-edge and Mo-edge and HDS efficiency, the S-edge/Mo-edge ratio and k_{DDS}/k_{HYD}.

Acknowledgements

This research was supported by the National Natural Science Foundation of China (No. 21878330, 21676298), the National Science and Technology Major Project, the CNPC Key Research Project (2016E-0707), and the King Abdullah University of Science and Technology (KAUST) Office of Sponsored Research (OSR) under Award (No. OSR-2019-CPF-4103.2).

Literature Cited

[1] Zhou, W.; Liu, M.; Zhang, Q.; Liu, M.; Wei, Q.; Ding, S.; Zhou, Y. Synthesis of NiMo Catalysts Supported on Gallium-Containing Mesoporous Y Zeolites with Different Gallium Contents and Their High Activities in the Hydrodesulfurization of 4,6-Dimethyldibenzothiophene. ACS Catal., 2017, 7, 7665-7679.

[2] Fan, Y.; Shi, G.; Bao, X. A process for producing ultraclean gasoline by coupling efficient hydrodesulfurization and directional olefin conversion. AIChE Journal, 2013, 59, 571-581.

[3] Wivel, C.; Clausen, B. S.; Candia, R.; Mørup, S.; Topsøe, H. Mössbauer emission studies of calcined $CoMoAl_2O_3$ catalysts: Catalytic significance of Co precursors. J.

Catal. 1984, 87, 497-513.

[4] Schweiger, H.; Raybaud, P.; Kresse, G.; Toulhoat, H. Shape and edge sites modifications of MoS_2 catalytic nanoparticles induced by working conditions: a theoretical study. J. Catal. 2002, 207, 76-87.

[5] Sun, Y.; Prins, R. Mechanistic studies and kinetics of the hydrodesulfurization of dibenzothiophene on Co-MoS_2/γ-Al_2O_3. J. Catal. 267, 193-201.

[6] Moses, P. G.; Hinnemann, B.; Topsøe, H.; Nørskov, J. K. The hydrogenation and direct desulfurization reaction pathway in thiophene hydrodesulfurization over MoS_2 catalysts at realistic conditions: A density functional study. J. Catal. 2007, 248, 188-203.

[7] Chen, J.; Maugé, F.; El Fallah, J.; Oliviero, L. IR spectroscopy evidence of MoS_2 morphology change by citric acid addition on MoS_2/Al_2O_3 catalysts - A step forward to differentiate the reactivity of M-edge and S-edge. 2014, 320, 170-179.

[8] Topsoe, N. Y.; Topsoe, H. FTIR studies of Mo/Al_2O_3-based catalysts: II. Evidence for the presence of SH groups and their role in acidity and activity. J. Catal. 1993, 139, 641-651.

[9] Han, W.; Nie, H.; Long, X.; Li, M.; Yang, Q.; Li, D. Preparation of F-doped MoS_2/Al_2O_3 catalysts as a way to understand the electronic effects of the support Brønsted acidity on HDN activity. J. Catal. 2016, 339, 135-142.

[10] Lauritsen, J. V.; Nyberg, M.; Nørskov, J. K.; Clausen, B. S.; Topsøe, H.; Lægsgaard, E.; Besenbacher, F. Hydrodesulfurization reaction pathways on MoS_2 nanoclusters revealed by scanning tunneling microscopy. J. Catal. 2004, 224, 94-106.

[11] Zhou, W.; Zhou, A.; Zhang, Y.; Zhang, C.; Chen, Z.; Liu, L.; Zhou, Y.; Wei, Q.; Tao, X. Hydrodesulfurization of 4, 6-dimethyldibenzothiophene over NiMo supported on Ga-modified Y zeolites catalysts. J. Catal. 2019, 374, 345-359.

[12] Chiu, J. J.; Pine, D. J.; Bishop, S. T.; Chmelka, B. F. Friedel-Crafts alkylation properties of aluminosilica SBA-15 meso/macroporous monoliths and mesoporous powders. J. Catal. 2004, 221, 400-412.

[13] Budi, C. S.; Saikia, D.; Chen, C. S.; Kao, H. M. Catalytic evaluation of tunable Ni nanoparticles embedded in organic functionalized 2D and 3D ordered mesoporous silicas from the hydrogenation of nitroarenes. J. Catal. 2019, 370, 274-288.

[14] Huirache-Acuña, R.; Zepeda, T. A.; Rivera-Muñoz, E. M.; Nava, R.; Loricera, C. V.; Pawelec, B. Characterization and HDS performance of sulfided CoMoW catalysts supported on mesoporous Al-SBA-16 substrates. Fuel 2015, 149, 149-161.

[15] Cao, Z.; Duan, A.; Zhao, Z.; Li, J.; Wei, Y.; Jiang, G.; Liu, J. A simple two-step method to synthesize the well-ordered mesoporous composite Ti-FDU-12 and its application in the hydrodesulfurization of DBT and 4, 6-DMDBT. J. Mater. Chem. A 2014, 2, 19738-19749.

[16] Morales-Ortuño, J. C.; Ortega-Domínguez, R. A.; Hernández-Hipólito, P.; Bokhimi, X.; Klimova, T. E. HDS performance of NiMo catalysts supported on nanostructured materials containing titania. Catal. Today 2016, 271, 127-139.

[17] Nguyen, T. T.; Qian, E. W. Synthesis of mesoporous Ti-inserted SBA-15 and CoMo/Ti-SBA-15 catalyst for hydrodesulfurization and hydrodearomatization. Microporous Mesoporous Mater. 2018, 265, 1-7.

[18] Garg, S.; Soni, K.; Kumaran, G. M.; Kumar, M.; Gupta, J. K.; Sharma, L. D.; Dhar, G. M. Effect of Zr-SBA-15 support on catalytic functionalities of Mo, CoMo, NiMo hydrotreating catalysts[J]. Catal. Today 2008, 130, 302-308.

[19] Berhault, G.; De la Rosa, M. P.; Mehta, A.; Yacaman, M. J.; Chianelli, R. R. The single-layered morphology of supported MoS_2-based catalysts-The role of the cobalt promoter and its effects in the hydrodesulfurization of dibenzothiophene. Appl. Catal.;

A 2008, 345, 80-88.

[20] Rodríguez, M. A.; Elizalde, I.; Ancheyta, J. Modeling the performance of a bench-scale reactor sustaining HDS and HDM of heavy crude oil at moderate conditions. Fuel, 2012, 100, 152-162.

[21] Gao, D.; Duan, A.; Zhang, X.; Zhao, Z.; E. H.; Li, J.; Wang, H.. Synthesis of NiMo catalysts supported on mesoporous Al-SBA-15 with different morphologies and their catalytic performance of DBT HDS, Appl. Catal. B: Environmental, 2015, 165, 269-284.

[22] Zhao, D.; Huo, Q.; Feng, J.; Chmelka, B. F.; Stucky, G. D.; Nonionic triblock and star diblock copolymer and oligomeric surfactant syntheses of highly ordered, hydrothermally stable, mesoporous silica structures, J. Am. Chem. Soc. 1998, 120, 6024-6036.

[23] Kumar, A.; Srinivas, D. Aminolysis of epoxides catalyzed by three-dimensional, mesoporous titanosilicates, Ti-SBA-12 and Ti-SBA-16. J. Catal. 2012, 293, 126-140.

[24] Dutoit, D. C. M.; Schneider, M.; Baiker, A. Titania-silica mixed oxides: I. Influence of sol-gel and drying conditions on structural properties. J. Catal. 1995, 153, 165-176.

[25] Liu, Y.; Cheng, B.; Wang, K.; Ling, G.; Cai, J.; Song, C.; Han, G. Study of Raman spectra for γ-Al_2O_3 models by using first-principles method. Solid State Commun. 2014, 178, 16-22.

[26] Riegel, B.; Hartmann, I.; Kiefer, W.; Groβ, J.; Fricke, J. Raman spectroscopy on silica aerogels. J. Non-Cryst. Solids 1997, 211, 294-298.

[27] Tompsett, G. A.; Bowmaker, G. A.; Cooney, R. P.; Metson, J. B.; Rodgers, K. A.; Seakins, J. M. The Raman spectrum of brookite, TiO_2 (PBCA, Z= 8). J. Raman Spectrosc. 1995, 26, 57-62.

[28] Bordiga, S.; Coluccia, S.; Lamberti, C.; Marchese, L.; Zecchina, A.; Boscherini, F.; Buffa, F.; Genoni, F.; Leofanti, G. XAFS Study of Ti-Silicalite: structure of framework Ti (IV) in the presence and absence of reactive molecules (H_2O, NH_3) and comparison with Ultraviolet-Visible and IR results. J. Phys. Chem. 1994, 98, 4125-4132.

[29] Marchese, L.; Gianotti, E.; Dellarocca, V.; Maschmeyer, T.; Rey, F.; Coluccia, S.; Thomas, J. M. Structure-functionality relationships of grafted Ti-MCM41 silicas. Spectroscopic and catalytic studies. Phys. Chem. Chem. Phys. 1999, 1, 585-592.

[30] Hu, Y.; Martra, G.; Zhang, J.; Higashimoto, S.; Coluccia, S.; Anpo, M. Characterization of the local structures of Ti-MCM-41 and their photocatalytic reactivity for the decomposition of NO into N_2 and O_2. J. Phys. Chem. B 2006, 110, 1680-1685.

[31] Blasco, T.; Corma, A.; Navarro, M. T.; Pariente, J. P. Synthesis, characterization, and catalytic activity of Ti-MCM-41 structures. J. Catal. 1995, 156, 65-74.

[32] Kormann, C.; Bahnemann, D. W.; Hoffmann, M. R. Preparation and characterization of quantum-size titanium dioxide. J. Phys. Chem. 1988, 92, 5196-5201.

[33] Klimova, T.; Lizama, L.; Amezcua, J. C.; Roquero, P.; Terrés, E.; Navarrete, J.; Domínguez, J. M. New NiMo catalysts supported on Al-containing SBA-16 for 4,6-DMDBT hydrodesulfurization: Effect of the alumination method. Catal. Today 2004, 98, 141-150.

[34] Zeng, S.; Blanchard, J.; Breysse, M.; Shi, Y.; Shu, X.; Nie, H.; Li, D. Post-synthesis alumination of SBA-15 in aqueous solution: A versatile tool for the preparation of acidic Al-SBA-15 supports. Microporous Mesoporous Mater. 2005, 85, 297-304.

[35] Reddy, B. M.; Chowdhury, B.; Reddy, E. P.; Fernández, A. X-ray photoelectron spectroscopy study of V_2O_5 dispersion on a nanosized Al_2O_3-TiO_2 mixed oxide. Langmuir 2001, 17, 1132-1137.

[36] Castillo, R.; Koch, B.; Ruiz, P.; Delmon, B. Influence of the amount of titania on the texture and structure of titania supported on silica. J. Catal. 1996, 161, 524-529.

[37] Matsumoto, R.; Nishizawa, Y.; Kataoka, N.; Tanaka, H.; Yoshikawa, H.; Tanuma, S.; Yoshihara, K. Reproducibility of XPS analysis for film thickness of SiO_2/Si by active Shirley method. J. Electron Spectrosc. Relat. Phenom. 2016, 207, 55-59.

[38] Dong, Z.; Ding, D.; Li, T.; Ning, C. High-efficiency photo electrochemical water splitting with heterojunction photoanode of In_2O_3-x nanorods/black Ti-Si-O nanotubes. Int. J. Hydrogen Energy. 2019, 44, 17611-17621.

[39] An, H.; Chen, Z.; Yang, J.; Feng, Z.; Wang, X.; Fan, F.; Li, C. An Operando-Raman study on oxygen evolution of manganese oxides: Roles of phase composition and amorphization. J. Catal. 2018, 367, 53-61.

[40] Mestl, G.; Srinivasan, T. K. K. Raman spectroscopy of monolayer-type catalysts: supported molybdenum oxides. Catal. Rev. 1998, 40, 451-570.

[41] Heegn, H.; Birkeneder, F.; Kamptner, A. Mechanical activation of precursors for nanocrystalline materials. Cryst. Res. Technol., 2003, 38, 7-20.

[42] Kim, D. S.; Wachs, I. E.; Segawa, K. Molecular structures and reactivity of supported molybdenum oxide catalysts. J. Catal. 1994, 149, 268-277.

[43] Williams, C. C.; Ekerdt, J. G.; Jehng, J. M.; Hardcastle, F. D.; Turek, A. M.; Wachs, I. E. A Raman and ultraviolet diffuse reflectance spectroscopic investigation of silica-supported molybdenum oxide. J. Phys. Chem. 1991, 95, 8781-8791.

[44] Qu, L.; Zhang, W.; Kooyman, P. J.; Prins, R. MAS NMR, TPR, and TEM studies of the interaction of NiMo with alumina and silica–alumina supports. J. Catal. 2003,

215, 7-13.

[45] Cordero, R. L.; Agudo, A. L. Effect of water extraction on the surface properties of Mo/Al_2O_3 and $NiMo/Al_2O_3$ hydrotreating catalysts. Appl. Catal., A 2000, 202, 23-35.

[46] Herrera, J. M.; Reyes, J.; Roquero, P.; Klimova, T. New hydrotreating NiMo catalysts supported on MCM-41 modified with phosphorus, Microporous Mesoporous Mater. 2005, 83, 283-291.

[47] Emeis, C. A. Determination of integrated molar extinction coefficients for infrared absorption bands of pyridine adsorbed on solid acid catalysts. J. Catal. 1993, 141, 347-354.

[48] Gallo, J. M. R.; Bisio, C.; Gatti, G.; Marchese, L.; Pastore, H. O. Physicochemical characterization and surface acid properties of mesoporous [Al]-SBA-15 obtained by direct synthesis. Langmuir 2010, 26, 5791-5800.

[49] Zakharova, M. V.; Kleitz, F.; Fontaine, F. G. Lewis acidity quantification and catalytic activity of Ti, Zr and Al-supported mesoporous silica. Dalton Trans. 2017, 46, 3864-3876.

[50] Wei, Z. B.; Yan, W.; Zhang, H.; Ren, T.; Xin, Q.; Li, Z. Hydrodesulfurization activity of $NiMo/TiO_2Al_2O_3$ catalysts. Appl. Catal., A 1998, 167, 39-48.

[51] Lai, W.; Song, W.; Pang, L.; Wu, Z.; Zheng, N.; Li, J.; Zheng, J.; Yi, X.; Fang, W.; The effect of starch addition on combustion synthesis of $NiMo\text{-}Al_2O_3$ catalysts for hydrodesulfurization. J. Catal. 2013, 303, 80-91.

[52] Mérida-Robles, J.; Rodŕıguez-Castellón, E.; Jiménez-López, A. Characterization of Ni, Mo and Ni-Mo catalysts supported on alumina-pillared α-zirconium phosphate and reactivity for the thiophene HDS reaction. J. Mol. Catal. A: Chem. 1999, 145, 169-181.

[53] Ishutenko, D.; Mozhaev, A.; Salnikov, V.; Nikulshin, P. Selective hydrodesulfurization of model fluid catalytic cracking gasoline over sulfided Al_2O_3-supported Anderson heteropolyoxomolybdate-based catalysts. React. Kinet. Mech. Cat. 2016, 119, 615-627.

[54] Vogelaar, B. M.; Kagami, N.; van der Zijden, T. F.; van Langeveld, A. D.; Eijsbouts, S.; Moulijn, J. A. Relation between sulfur coordination of active sites and HDS activity for Mo and NiMo catalysts. J. Mol. Catal. A: Chem. 2009, 309, 79-88.

[55] Travert, A.; Dujardin, C.; Maugé, F.; Veilly, E.; Cristol, S.; Paul, J. F.; Payen, E. CO adsorption on CoMo and NiMo sulfide catalysts: a combined IR and DFT study. J. Phys. Chem. B 2006, 110, 1261-1270.

[56] Labruyere, V. Structure des sites sulfures des catalyseurs d'hydrotraitement: approche combinee par spcetroscopie IR et modelisation moleculaire, in, universite de Caen, 2014.

[57] Zepeda, T. A.; Fierro, J. L. G.; Pawelec, B.; Nava, R.; Klimova, T.; Fuentes, G. A.; Halachev, T. Synthesis and characterization of Ti-HMS and CoMo/Ti-HMS oxide materials with varying Ti content. Chem. Mater. 2005, 17, 4062-4073.

[58] Huang, T.; Xu, J.; Fan, Y. Effects of concentration and microstructure of active phases on the selective hydrodesulfurization performance of sulfided $CoMo/Al_2O_3$ catalysts. Appl. Catal., B 2018, 220, 42-56.

[59] Paul, J. F.; Payen, E. Vacancy formation on MoS_2 hydrodesulfurization catalyst: DFT study of the mechanism. J. Phys. Chem. B 2003, 107, 4057-4064.